Wideband micromachined capacitive microphones with radio frequency detection

Sean T. Hansen,[a] A. Sanli Ergun, William Liou, Bertram A. Auld, and Butrus T. Khuri-Yakub
Edward L. Ginzton Laboratory, Stanford University, Stanford, California 94305-4088

(Received 19 December 2003; revised 2 April 2004; accepted 21 May 2004)

Silicon microphones based on capacitive micromachined ultrasonic transducer membranes and radio frequency detection overcome many of the limitations in bandwidth, uniformity of response, and durability associated with micromachined condenser microphones. These membranes are vacuum-sealed to withstand submersion in water and have a flat mechanical response from dc up to ultrasonic frequencies. However, a sensitive radio frequency detection scheme is necessary to detect the small changes in membrane displacement that result from utilizing small membranes. In this paper we develop a mathematical model for calculating the expected output signal and noise level and verifies the model with measurements on a fabricated microphone. Measurements on a sensor with 1.3 mm^2 area demonstrate less than 0.5 dB variation in the output response between 0.1 Hz to 100 kHz under electrostatic actuation and an A-weighted equivalent noise level of 63.6 dB(A) SPL in the audio band. Because the vacuum-sealed membrane structure has a low mechanical noise floor, there is the potential for improved sensitivity using higher carrier frequencies and more sophisticated detection circuitry.
[DOI: 10.1121/1.1771617]

PACS numbers: 43.38.Gy, 43.38.Kb [AJZ] Pages: 828–842

I. INTRODUCTION

The demand for inexpensive microphones, coupled with advancements in silicon micromachining technology, has led to the development of many miniature acoustic pressure sensors.[1] The development of miniature microphones primarily has focused on hearing aid applications, and therefore concentrates on acoustic detection only in a limited audio range.[2] However, some scientific, industrial, and military applications require acoustic data collection over a broader bandwidth for proper signal identification. Frequencies above 25 kHz contain useful information for condition-monitoring applications, particularly for machining and welding processes.[3] Acoustic sensing below the audio range is useful for target tracking and monitoring of heavy equipment and engines,[4,5] as well as for studying infrasonic geophysical phenomena.[6,7] In addition, unattended operation in harsh outdoor environments requires sensors that are impervious to dust and moisture. While certain measurement microphones have the necessary bandwidth and durability for such applications, the high cost of precision instruments can be a barrier to their widespread use. A micromachined silicon sensor is therefore desirable, as micromachining and lithography techniques offer the prospect of inexpensive, mass-produced acoustic sensors and sensor arrays.

A durable, wideband micromachined microphone is possible using ultrasonic membranes that are vacuum-sealed. To maintain sensitivity, a radio frequency (rf) detection technique senses the changes in membrane capacitance in order to recover the acoustic signal. Applying rf techniques to measure changes in microphone capacitance is not new. Zuckerwar[8] and Hibbings[9] describe several rf techniques that have been applied to microphones. Most of these systems incorporate a condenser cartridge in a resonator and measure the resulting amplitude, frequency, or phase modulation of an oscillator signal. Ergun *et al.*[10,11] recently proposed an acoustic sensor using an alternative rf technique, in which capacitance variations were detected through the phase modulation of a rf carrier signal along a capacitively loaded transmission line. This technique, henceforth referred to as rf detection, elegantly applies to a capacitive transducer consisting of multiple small cells. Following a general description of the microphone's mechanical structure and the rf detection technique, we develop a mathematical model for simulating its performance using rf detection. A comparison of the predictions and experimental measurements is followed by a discussion of the model and the potential capabilities of the microphone. To highlight the differences between this sensor and other common microphone approaches, we begin with an overview of micromachined condenser microphones.

II. MICROMACHINED CONDENSER MICROPHONES

A. Conventional microphone membranes

Many micromachined condenser microphones use a similar membrane structure to that of large measurement microphones and studio recording microphones. One common structure for omnidirectional pressure microphones, shown in Fig. 1, consists of a conductive membrane suspended over a conductive backplate that is perforated with holes for acoustic damping. Sound detection is possible when the impinging pressure wave vibrates the membrane, thus changing the capacitance of the transducer. Under normal operation,

[a]Electronic mail: sthansen@piezo.stanford.edu

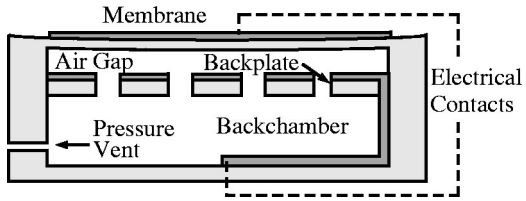

FIG. 1. Cross-sectional structure of a condenser microphone.

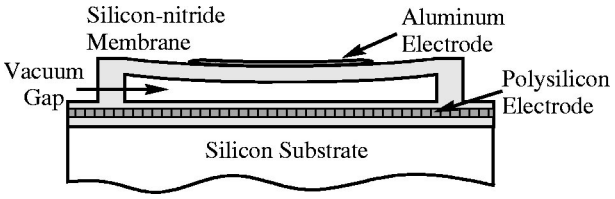

FIG. 3. Cross-sectional structure of a single CMUT membrane.

the electrodes of the capacitor are charged using an external voltage bias through a large resistor. The changes in capacitance of the membrane are translated into changes in voltage, which can be sensed using a high-impedance preamplifier. A pressure equalization vent in the backchamber prevents fluctuations in atmospheric pressure from collapsing the membrane against the backplate.

A precision condenser microphone for measurement or calibration applications is capable of a uniform frequency response due to its relatively large air gap, on the order of 20 μm, behind the membrane.[2] Silicon micromachined microphones, with membrane dimensions of 1–2 mm, require air gaps on the order of a few microns to maintain adequate sensitivity due to the reduced motion that results from a smaller membrane. However, the reduced dimensions of the air gap magnify the effects of squeeze-film damping, introducing frequency-dependent stiffness and loss.[1] This creates undesirable variations in the mechanical response with acoustic frequency. Furthermore, achieving a large dynamic range and a high sensitivity can be conflicting goals, since large sound pressures may cause the membrane to collapse under its voltage bias.[12]

Beranek[13] derives a small-signal acoustic equivalent circuit model for condenser microphones that can be applied to micromachined microphones of a similar structure. This model, shown in Fig. 2, includes additional elements to model the effects of the pressure equalization vent, discussed by Scheeper.[14] Due to the difficulty of fabricating a vent with high acoustic impedance using silicon micromachining technology, low-frequency acoustic signals at the membrane are partially equalized. This reduces the net pressure differential between the two sides of the membrane and results in a low-frequency mechanical roll-off in the membrane response.[8] The vent not only influences the directionality of the microphone, but also prevents many micromachined microphones from sensing below 100 Hz, an important range for military acoustic applications. Finally, miniature condenser microphones can be susceptible to condensation in the narrow air gaps when exposed to humid environments or sudden temperature changes.[2] Moisture in the air gap can hinder membrane movement and may require regular cleaning to remove.

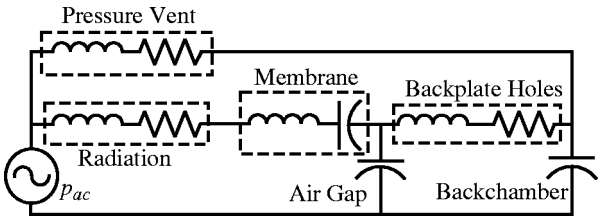

FIG. 2. Acoustic small-signal equivalent circuit representation of the microphone structure in Fig. 1. The harmonic pressure amplitude p_{ac} is that at the membrane surface when it is restrained from moving.

B. The sealed CMUT membrane

An alternative membrane structure that overcomes many of the drawbacks of conventional capacitive micromachined microphone designs incorporates many smaller vacuum-sealed membranes. Capacitive micromachined ultrasonic transducers (CMUTs), which have been developed for the generation and reception of ultrasound in air and water,[15,16] can be used in microphones. The structure of a single CMUT membrane, shown in Fig. 3, consists of a metallized circular or rectangular silicon nitride membrane suspended over a silicon substrate. A typical membrane thickness is less than 1 μm, while lateral dimensions range from tens of microns to 100 μm. Because the individual membranes are small, tens or hundreds of them are electrically connected to form a transducer for the generation or reception of acoustic waves.

A CMUT membrane is smaller and stiffer than a conventional condenser microphone membrane, which permits vacuum sealing of the volume behind the membrane. The vacuum-sealed membrane structure has many important implications for microphone performance. First, the absence of air and a perforated backplate in the CMUT structure simplifies its equivalent circuit model, which is shown in Fig. 4. This model can be derived from that of the condenser microphone by noting that the stiffness of the air behind the membrane is zero in vacuum, thereby shorting the capacitors that represent the air gap and backchamber in the equivalent circuit of Fig. 2. In addition, the resistors that model the air flow through the backplate holes and pressure vent become open circuits, as there is no pathway for the flow of air behind the membrane. Therefore, squeeze-film damping, which is usually the dominant source of noise in condenser microphones over most of the audio range,[17] is eliminated. The absence of frequency-dependent circuit elements of the backchamber and pressure equalization vents in the circuit model suggests that the uniformity of the frequency response is also improved. Unlike standard unsealed microphones, the sealed CMUT structure does not have a low-frequency acoustic

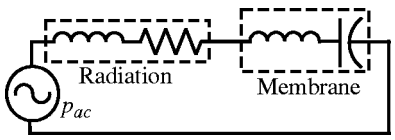

FIG. 4. Acoustic small-signal equivalent circuit representation of one or more CMUT membranes.

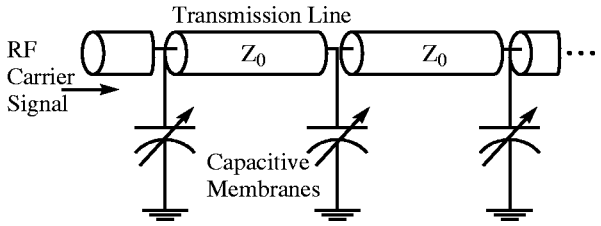

FIG. 5. In rf detection, the capacitive membranes periodically load a transmission line. A rf carrier signal experiences a phase shift with the changing capacitance.

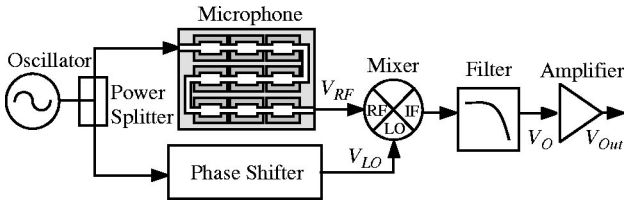

FIG. 6. Block diagram showing the microphone as part of a phase detection circuit that recovers the acoustic signal incident on the microphone.

roll-off and responds to excitations at arbitrarily low frequencies, including atmospheric pressure fluctuations.

Because small CMUT membranes resonate at frequencies greater than several hundred kilohertz, the spring compliance of the membrane, represented by a capacitor in the equivalent circuit, dominates its response for the frequencies of interest. Therefore, the displacement response of the membrane is flat below its resonant frequency. Finally, the durability of the microphone is improved because the hermetic structure prevents condensation and particle contamination from getting inside the narrow capacitor gaps and hindering membrane motion. Experimental measurements in air confirm that such microphones are not affected by prior submersion in water. In fact, we confirm that the sensor can operate as a hydrophone in a liquid medium.

Condenser microphone systems measure capacitance changes, which are approximately a linear function of the membrane displacement due to acoustic pressure. For a circular membrane, the low-frequency displacement response is roughly proportional to its area.[8] Therefore, the use of N small CMUT membranes, rather than a single membrane of the same total area, reduces the displacement and the expected change in capacitance by a factor of N. This illustrates the primary tradeoff for the uniform, durable response provided by small CMUT membranes. Fortunately, the expected mechanical noise level of the sealed CMUT structure is extremely low, which suggests that a sensitive microphone remains possible. A rf detection technique compensates for the small displacement response of the membranes with a sensitive method for detecting slight capacitance changes.

III. RADIO FREQUENCY DETECTION WITH CAPACITIVE MEMBRANES

A. Description

In rf detection, tens or hundreds of capacitive membranes are periodically spaced along a rf transmission line, creating a capacitively loaded transmission line, as shown in Fig. 5. This structure acts as a filter for millimeter-wave microwave signals, but still behaves as a transmission line for rf signals within its passband.[18] As the capacitive membranes in the line vibrate due to sound pressure, the transmission line's propagation constant, or equivalently, the phase velocity of the rf signal, also changes. Thus, a rf carrier signal that is launched down the loaded transmission line is phase modulated by the acoustic signal that impinges on the capacitive membranes. Subsequent demodulation using a phase detection circuit recovers the acoustic signal.

B. Circuitry

The phase modulation of the rf carrier can be sensed when the microphone is included as part of a phase detection circuit, such as the one shown in Fig. 6, commonly used to detect phase variations in electrical devices.[19] The circuit first splits the rf signal from an oscillator into two branches. One branch passes through the microphone, which phase modulates the rf signal by the acoustic signal on the CMUT membranes. Mathematically, this signal takes the form

$$V_{\mathrm{rf}} = V_1 \cos(2\pi f_c t + \Phi(t)), \tag{1}$$

where V_1 and f_c are the amplitude and frequency of the rf carrier, respectively, and $\Phi(t)$ represents some time-varying phase modulation due to an acoustic signal. The second branch transfers a reference signal to the local oscillator (LO) port of the mixer,

$$V_{\mathrm{LO}} = V_2 \cos(2\pi f_c t + \phi), \tag{2}$$

where V_2 is the amplitude of the voltage signal and ϕ represents some fixed phase relative to the signal V_{rf}. Ideally, the mixer performs multiplication of the signals at its input ports, resulting in output components at the sum and difference of the input frequencies:

$$V_{\mathrm{rf}} \times V_{\mathrm{LO}} = K_d[\cos(\Phi(t) - \phi) + \underbrace{\cos(4\pi f_c t + \Phi(t) + \phi)}_{\text{removed by low-pass filter}}]. \tag{3}$$

These signals have a new voltage amplitude K_d due to losses during mixing. A low-pass filter at the mixer output removes the component of the signal at twice the carrier frequency, $2f_c$, as well as any additional higher-order harmonics that may be generated. The demodulated (or baseband) signal,

$$V_O = K_d \cos(\Phi(t) - \phi), \tag{4}$$

consists of a phase varying term $\Phi(t)$ and a fixed phase reference ϕ. If ϕ is adjusted to $\pi/2$ rad so that the two signals at the mixer inputs are in quadrature, the demodulated signal V_O is proportional to the small phase variations of $\Phi(t)$:

$$V_O = K_d \sin(\Phi(t)) \approx K_d \Phi(t). \tag{5}$$

Because $\Phi(t)$ is proportional to the change in capacitance, recovering $\Phi(t)$ recovers the acoustic pressure signal on the membranes. The scaling term K_d, with units of V/rad, acts as a phase detection constant for the mixer that converts radian phase shifts of the rf carrier into a baseband voltage signal. Additional amplification increases the signal to the desired level.

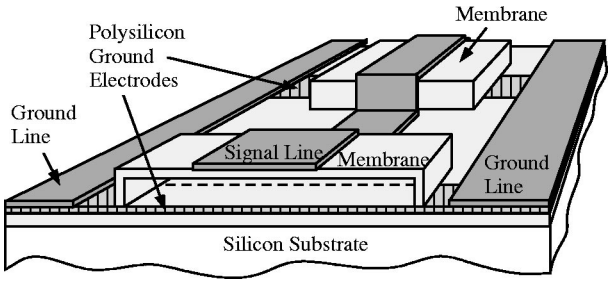

FIG. 7. The signal line of a coplanar waveguide transmission line traverses the rectangular CMUT membranes. Doped polysilicon electrodes extend underneath a portion of the membrane and connect to the ground conductors of the transmission line.

Although more complicated than the constant voltage detection systems usually applied to condenser microphones, the rf detection system has some distinct advantages. First, the parasitic capacitance between membrane cells due to interconnects is incorporated into the rf transmission line structure. This is particularly relevant for a microphone composed of many small capacitors such as CMUTs, because parasitic capacitance degrades the sensitivity of the microphone in constant voltage detection.[8] A dc voltage bias is not required for operation, although a voltage can be applied to the membranes to adjust their deflection with changes in atmospheric pressure and to alter the microphone's sensitivity or calibration. In addition, the output impedance of the mixer in rf detection is low, typically around 50 Ω, so an amplifier with a high-impedance input is unnecessary. Because the output is independent of acoustic frequency variations in $\Phi(t)$, the low-frequency response of the CMUT structure is preserved for a broadband microphone. As a consequence, the circuit in Fig. 6 responds to shifts in atmospheric pressure or slow drifts in the electrical components. Therefore, a practical implementation uses feedback, applied through a voltage-controlled phase shifter or a variable voltage bias on the membranes, to nullify such offsets over the long term. Thus, the minimum detectable acoustic frequency of the system becomes selectable through the time constant of the feedback signal.

C. Sensor fabrication

The transmission line structure of Fig. 5 is implemented using a coplanar waveguide transmission line over CMUT membranes. Similar capacitively loaded structures with a coplanar waveguide have been fabricated for microwave phase shifters using voltage-actuated metal bridges[20] instead of enclosed membranes. The final structure of the microphone for rf detection, shown in Fig. 7, consists of a series of surface-micromachined membranes covered by a coplanar waveguide transmission line, which consists of three conductors: a center signal line that traverses the membranes and one ground line on either side of a row of membranes. The lower electrode of each capacitive membrane is formed by a locally doped polysilicon layer that extends underneath the center portion of the membrane to the ground lines. Polysilicon is used for this conductor instead of metal because the high deposition temperature of silicon nitride for the membrane exceeds the melting temperatures of common metals.

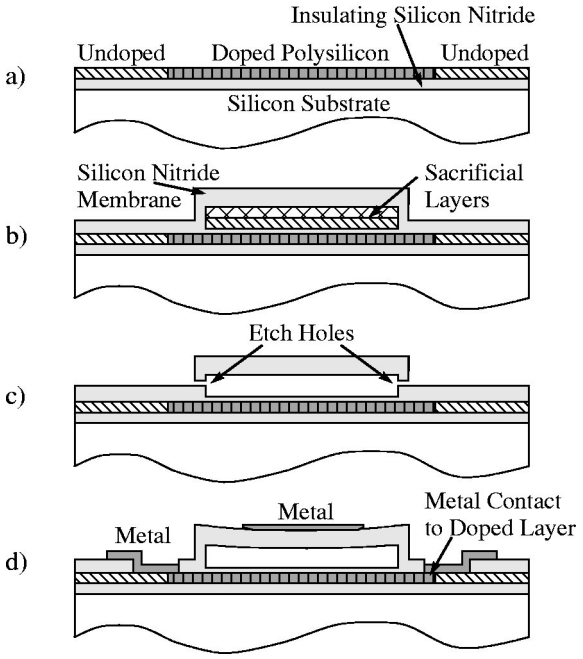

FIG. 8. Cross-sections showing selected fabrication steps of CMUT membranes for use in rf detection. The relevant dimensions of the fabricated microphone are presented in subsequent sections.

The absence of the perforated backplate and capillary tube for pressure equalization, which are usually found in other micromachined condenser structures, simplifies the fabrication of the membranes. The processing steps for the sealed CMUT membrane are similar to those described by Jin,[21] with a few differences for rf detection. We start with an insulating, high-resistivity (2000 Ω cm) silicon substrate, which is suitable for low-loss coplanar transmission lines at several gigahertz.[22] The silicon substrate is coated with insulating films of silicon nitride and polysilicon, both deposited using low-pressure chemical vapor deposition (LPCVD). Sections of the polysilicon layer under the membranes are doped in a high-temperature furnace with phosphorous oxychloride using silicon dioxide to mask areas of the polysilicon that should act as electrical insulators. Figure 8(a) shows the structure after removing the silicon dioxide mask in hydrofluoric acid. Following a thin silicon nitride deposition, which serves as an etch stop, the membrane structure is formed by depositing silicon nitride over patterned sacrificial layers of polysilicon and low-temperature silicon dioxide, as shown in Fig. 8(b). Small via holes are plasma etched at the side of the silicon nitride membrane, which permit the subsequent wet etch of the sacrifical layers to release the membrane. The etch is accomplished with a solution of potassium hydroxide followed by hydrofluoric acid, producing the membrane structure of Fig. 8(c). A second deposition of silicon nitride seals the etch holes, and because the deposition occurs in a vacuum furnace, the membrane structure is vacuum-sealed. The sealed silicon nitride membrane is etched to its final thickness to obtain the desired stiffness and deflection under atmospheric pressure. A plasma-etch opens contacts to the doped polysilicon electrode that extends underneath the membrane. Finally, Fig. 8(d) shows the complete structure after patterning the metal transmission lines of sputtered alu-

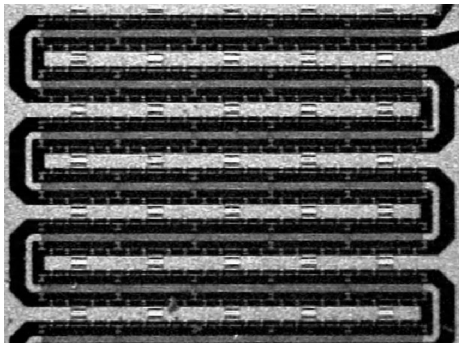

FIG. 9. Microscope photograph showing a portion of the fabricated 1.3 mm^2 microphone, formed by snaking a transmission line over an array of 45 rectangular CMUT membranes, each 70 μm by 190 μm in size.

minum. The fabricated microphone die is mounted and wire bonded to a printed circuit board that has connectors to interface with the detection electronics. An optional coating of parylene can provide electrical insulation between the transmission line conductors if the microphone is operated in water.

IV. A MATHEMATICAL MODEL

The development of a mathematical model of a microphone using CMUTs and rf detection is essential to explore the potential capabilities and design tradeoffs of the sensor. Microphone sensitivity, one of the most important specifications for a microphone, is traditionally described in terms of the output voltage for an incident pressure. While this figure is useful for describing a condenser cartridge with or without a preamplifier, it is not straightforward to apply this measure to rf detection since the microphone and detection circuitry are interdependent. Furthermore, the use of voltage per pressure to describe the sensitivity of a rf detection system is misleading since subsequent amplification increases the output voltage without any apparent tradeoffs. A measure of sensitivity also should provide information about the minimum detectable sound pressure of the microphone, and, therefore, should incorporate both electrical and mechanical noise sources. Thus, the output signal-to-noise ratio (SNR) is a convenient measure of microphone sensitivity, and it is not limited to any particular frequency range. This ratio compares the rms signal voltage and rms noise voltage at the system output for a given frequency, noise bandwidth, and incident pressure.

The following sections develop a model to calculate the signal and noise levels necessary to predict microphone sensitivity. Sample calculations using the parameters for the fabricated microphone, shown in Fig. 9, are compared to experimental results in Sec. V. In both the simulation and the experimental measurements, the phase detection circuit of Fig. 6 consists of the following components: a free-running dielectric resonator oscillator (EMF Systems model 52747-512086) with 20 dBm of output power at 2.8 GHz, a reactive power splitter (Minicircuits model ZAPDQ-4), a mechanical phase shifter (ARRA model L9428A), a double-balanced mixer (Marki Microwave model M1-0204NA), a low-pass filter (Minicircuits model SLP-1.9), and a baseband amplifier using an operational amplifier (Analog Devices model AD797). Values for the relevant parameters associated with the fabricated microphone and its phase detection circuit are presented as needed in the model development. For parameters that are measured directly from the fabricated microphone, the number of significant digits indicates the estimated precision of the measurement.

A. Membrane response

The first step in modeling the output signal of the microphone in a phase detection circuit involves the calculation of the membrane movement in response to the pressure at its surface. As the acoustic equivalent circuit for the vacuum-sealed CMUT does not contain any acoustic elements behind the membrane that influences its motion, the analysis is simpler than for unsealed microphones. However, the microphone's size and packaging can influence its response at high frequencies, where the wavelength of sound in air approaches the size of the microphone.[23] To separate the effects of packaging from the analysis, the starting point for analyzing membrane motion is the pressure at the membrane surface. For frequencies at which the sensor and its packaging are much smaller than the wavelength of sound in fluid, diffraction effects are negligible and the pressure signal at the diaphragm surface is approximately the same as would exist in free-field conditions.[23]

Both the membrane deflection under static (dc) pressure and the movement of the membrane under harmonic (ac) pressures are considered. Although a CMUT membrane is a compound structure consisting of partially metalized silicon nitride, measurements of membrane deflection under atmospheric pressure before and after metallization usually differ by less than 2%. Therefore, the silicon nitride membrane dominates the stiffness of the structure, and the effects of the metal are neglected in the model.

Mason[24] derives a general equation of motion for a uniform stretched diaphragm, shown with slight modifications to the notation:

$$D\nabla^4 u - l_m \sigma \nabla^2 u - p + l_m \rho \frac{\partial^2 u}{\partial t^2} = 0. \tag{6}$$

Here, u is the vertical or transverse displacement, l_m is the membrane thickness, p is either the static or acoustic pressure, σ is the residual stress, and ρ is the density of the membrane material. Although we continue to use the common term *membrane* throughout the following analysis, the precise structure modeled by Eq. (6) is a *stretched diaphragm* since both the bending stiffness of a finite-thickness plate and the residual tensile stress of the material are included. The flexural rigidity D in Eq. (6) is given by

$$D = \frac{E l_m^3}{12(1-\upsilon^2)}, \tag{7}$$

where E is the Young's modulus, and υ is the Poisson's ratio of the material.[24]

A rectangular membrane geometry is used in the fabricated microphone because its peak displacement is greater than that of the inscribed circular membrane of the same

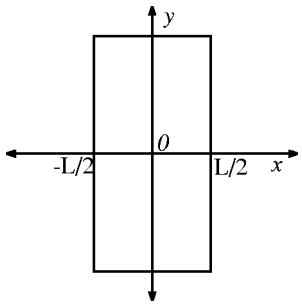

FIG. 10. Coordinate system and top view of the membrane orientation for a mathematical analysis.

thickness. For rectangular membranes, it is convenient to analyze the equation in Cartesian spatial coordinates (x,y), so the ∇^2 and ∇^4 operators are

$$\nabla^2=\left(\frac{\partial^2}{\partial x^2}+\frac{\partial^2}{\partial y^2}\right)$$

and

$$\nabla^4=\left(\frac{\partial^2}{\partial x^2}+\frac{\partial^2}{\partial y^2}\right)\left(\frac{\partial^2}{\partial x^2}+\frac{\partial^2}{\partial y^2}\right).$$

Following the approach of Badi *et al.*,[25] the complexity of the partial differential equation is reduced considerably by treating the rectangular membrane as very long in one dimension and taking the other dimension to be length L. Treating the displacement u only as a function of time and the x coordinate in Fig. 10, Eq. (6) becomes

$$Du''''(x,t)-l_m\sigma u''(x,t)-p+l_m\rho\ddot{u}(x,t)=0, \tag{8}$$

where $u'(x,t)$ denotes a spatial derivative, and $\dot{u}(x,t)$ denotes a time derivative of $u(x,t)$.

For the case of dc deflection under atmospheric pressure p_{dc}, the time variations in u are negligible, reducing Eq. (8) to a fourth-order ordinary differential equation for $u(x)$:

$$Du''''(x)-l_m\sigma u''(x)=p_{\mathrm{dc}}. \tag{9}$$

The general solution of the equation for the static displacement $u_{\mathrm{dc}}(x)$ is

$$u_{\mathrm{dc}}(x)=c_1+c_2x+c_3e^{\sqrt{l_m\sigma/D}x}+c_4e^{-\sqrt{l_m\sigma/D}x}-\frac{p_{\mathrm{dc}}}{2l_m\sigma}x^2. \tag{10}$$

The four unknown constants are found by applying the boundary conditions for a clamped plate, specifically that $u_{\mathrm{dc}}(x)$ and $u'_{\mathrm{dc}}(x)$ are zero at the edges of the diaphragm, where $x=\pm L/2$. Due to the symmetry of the coordinate system of Fig. 10, c_3 and c_4 are identical and c_2 is zero in Eq. (10). Redefining the constants and applying the boundary conditions yields the solution for the static deflection under pressure p_{dc}:

$$u_{\mathrm{dc}}(x)=\frac{p_{\mathrm{dc}}}{2l_m\sigma}\left[c'_1-x^2+c'_{3,4}\cosh\left(\sqrt{\frac{l_m\sigma}{D}}x\right)\right], \tag{11}$$

where

TABLE I. Dimensions and parameters of the CMUT membranes in the fabricated microphone.

Parameter	Symbol	Value
Length	L	70 μm
Width	W	190 μm
Thickness[a]	l_m	0.40 μm
Residual stress[a]	σ	1.1×10^8 Pa
Young's modulus[b]	E	3.2×10^{11} Pa
Density[b]	ρ	3270 kg/m^3
Poisson's ratio[b]	v	0.26
Atmospheric (dc) pressure	p_{dc}	1.01×10^5 Pa
Pressure (ac) amplitude	p_{ac}	1.41 Pa (=1 Pa rms)

[a]Measured from the fabricated microphone.
[b]Taken from Appendix B of Kino (Ref. 41) for silicon nitride.

$$c'_1=\frac{L^2}{4}-L\sqrt{\frac{D}{l_m\sigma}}\coth\left(\frac{L}{2}\sqrt{\frac{l_m\sigma}{D}}\right)$$

and

$$c'_{3,4}=L\sqrt{\frac{D}{l_m\sigma}}\operatorname{csch}\left(\frac{L}{2}\sqrt{\frac{l_m\sigma}{D}}\right).$$

This result is used later to calculate the static capacitance of the vacuum-sealed capacitive membranes under atmospheric pressure. Using the parameters from the fabricated microphone membranes, shown in Table I, Eq. (11) predicts 0.895 μm deflection at the membrane center $(x=0)$ under standard atmospheric pressure.

The response of the membrane to time-varying pressure is similarly calculated from Eq. (8). For a time-harmonic pressure amplitude of p_{ac} at angular acoustic frequency ω_a, the second-order time derivative scales u by $-\omega_a^2$. Thus, at a fixed excitation frequency, Eq. (8) reduces to an ordinary differential equation in a single variable:

$$Du''''(x)-l_m\sigma u''(x)-l_m\rho\omega_a^2u(x)=p_{\mathrm{ac}}. \tag{12}$$

The solution for harmonic excitation is obtained by finding a general solution and then applying the same clamped boundary conditions as in the static case to solve for the unknown constants. Following this procedure, the solution for amplitude of the ac displacement $u_{\mathrm{ac}}(x)$ is

$$u_{\mathrm{ac}}(x)=\frac{p_{\mathrm{ac}}}{\rho l_m\omega_a^2}[c_{1,2}\cosh(k_1x)+c_3\cos(k_3x)-1], \tag{13}$$

where

$$k_1=\sqrt{\frac{l_m\sigma+\sqrt{l_m^2\sigma^2+4Dl_m\rho\omega_a^2}}{2D}},$$

$$k_3=\sqrt{\frac{-l_m\sigma+\sqrt{l_m^2\sigma^2+4Dl_m\rho\omega_a^2}}{2D}},$$

$$c_{1,2}=\frac{k_3\sin(k_3L/2)}{k_1\sinh(k_1L/2)\cos(k_3L/2)+k_3\cosh(k_1L/2)\sin(k_3L/2)},$$

and

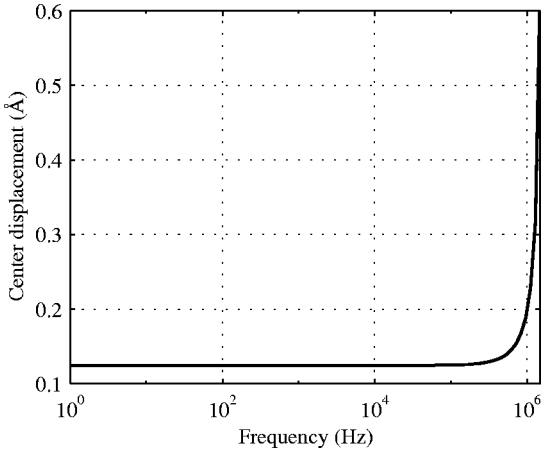

FIG. 11. The simulated displacement amplitude u_{ac} at the membrane center using Eq. (13) and the values given in Table I.

$$c_3 = \frac{k_1 \sinh(k_1 L/2)}{k_1 \sinh(k_1 L/2)\cos(k_3 L/2) + k_3 \cosh(k_1 L/2)\sin(k_3 L/2)}.$$

The ac motion at the center of a membrane with the dimensions and parameters of Table I is simulated in Fig. 11. As suggested earlier, the predicted displacement amplitude of 0.124 Å for 1.41 Pa amplitude ac pressure (or equivalently, 1 Pa rms) is extremely small, due to the miniature lateral dimensions of the membrane. Below 1 MHz, the membrane response does not vary appreciably from its low-frequency value. Because the membrane resonance is significantly greater than the usable frequency range of the microphone, the solution for the static deflection can be used to calculate the low-frequency harmonic excitation in most cases. Indeed, the static and dynamic solutions shown in Eq. (11) and Eq. (13) converge below the membrane resonant frequency for the same pressure input. Because the equations and solutions presented here for membrane displacement are linear with applied pressure, the previous analysis implicitly assumes that the dc deflection of the membrane under atmospheric pressure does not influence the ac response of the membrane to acoustic pressure signals. This assumption is a potential source of error in the model, as large deformations of the membrane likely stiffen the structure, reducing its ac response.

B. Capacitance calculations

Once the membrane response is characterized, it is straightforward to calculate the capacitances that load the transmission line in rf detection. The capacitance C_m between the top metal electrode and the ground electrode beneath the membrane, neglecting fringing fields near the conductor edges, is calculated by integrating the parallel-plate capacitance formula with two dielectrics over the area of overlap of the electrodes:

$$C_m = \int\int_{Area} \frac{\epsilon_m \epsilon_0}{l_m + l_i + \epsilon_m l_g(x,y)}\, dx\, dy. \tag{14}$$

Here, l_g is the effective vacuum gap between the membrane and substrate with free-space permittivity ϵ_0, and l_m is the thickness of the membrane material with relative permittivity ϵ_m. The small insulation thickness l_i of silicon nitride, shown in Fig. 12 over the ground electrode, adds directly to the membrane dielectric thickness in the capacitance formula. The vacuum gap l_g is shown as a function of position to indicate that the size of the gap changes with coordinate position because of the membrane's deflection under atmospheric pressure. Since the expression for u_{dc} is a function of x position only, the integration over area can be simplified to a single integral by neglecting the y-coordinate variations. Based on the geometries shown in Figs. 12 and 13, the capacitance of a membrane with metal electrode width w_m and ground electrode width w_g is

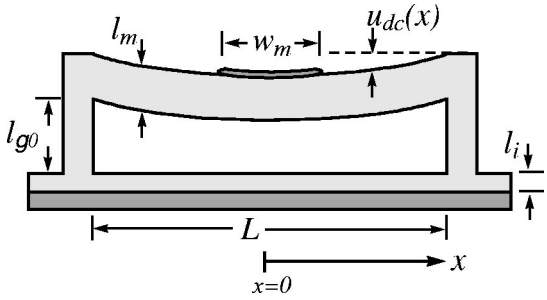

FIG. 12. Labeled schematic cross-section of a membrane, taken along the x coordinate axis of Fig. 10.

$$C_m = \int_{-w_m/2}^{w_m/2} \frac{w_g \epsilon_m \epsilon_0}{l_m + l_i + \epsilon_m (l_{g0} - u_{dc}(x))}\, dx, \tag{15}$$

where the gap l_g is replaced by the difference between the initial zero-deflection gap l_{g0} and the membrane static deflection $u_{dc}(x)$. Following the calculation of $u_{dc}(x)$ using Eq. (11), the integral of Eq. (15) can be evaluated numerically to calculate the static membrane capacitance.

The capacitance due to an incremental acoustic pressure is found by superimposing the membrane's ac displacement $u_{ac}(x)$ onto its static deflection in the capacitance formula:

$$C_{dc+ac} = \int_{-w_m/2}^{w_m/2} \frac{w_g \epsilon_m \epsilon_0}{l_m + l_i + \epsilon_m (l_{g0} - u_{dc}(x) - u_{ac}(x))}\, dx. \tag{16}$$

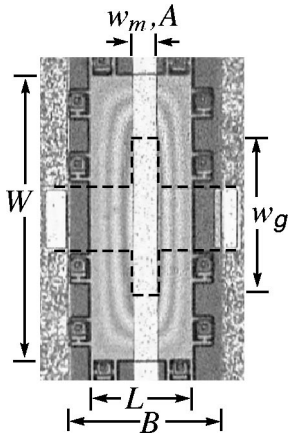

FIG. 13. Labeled photograph (top view) of a single membrane from the fabricated microphone. The dashed lines indicate the shape and extent of the polysilicon ground electrode under the membrane.

TABLE II. Additional parameters and dimensions of the fabricated CMUT membrane for capacitance calculations.

Parameter	Symbol	Value
Metal electrode width	w_m	20 μm
Ground electrode width	w_g	100 μm
Initial vacuum gap[a]	l_{g0}	1.00 μm
Insulation thickness[a]	l_i	0.10 μm
Membrane relative permittivity[a]	ϵ_m	5.7
Free-space permittivity	ϵ_0	8.854×10^{-12} F/m

[a]Measured from the fabricated microphone.

Finally, the change in membrane capacitance ΔC_m due to the ac pressure is calculated by subtracting the static membrane capacitance C_m from the capacitance under both static and acoustic pressures $C_{\mathrm{dc+ac}}$:

$$\Delta C_m = C_{\mathrm{dc+ac}} - C_m . \tag{17}$$

Using the parameters in Table II, the predicted static capacitance of a membrane from the fabricated microphone is 79 fF using the calculated static deflection under atmospheric pressure. The amplitude of the changing capacitance ΔC_m of a single membrane is 4.3 aF for the calculated displacement amplitude of 0.124 Å associated with a 1 Pa rms pressure signal. These values are used in the following section to calculate the phase shift of the microphone transmission line in rf detection.

C. Transmission line with capacitive loading

As previously described, rf detection senses the phase shift of a carrier signal at frequency f_c through a transmission line loaded with capacitive membranes. Before modeling the effects of capacitive loading, the characterization of the unloaded transmission line is necessary. Wen[26] derives an expression for the capacitance per unit length C_t of a coplanar waveguide transmission line:

$$C_t = 4\epsilon_{\mathrm{eff}}\epsilon_0 \frac{K(k)}{K(k')}, \tag{18}$$

where

$$\epsilon_{\mathrm{eff}} = (\epsilon_{\mathrm{sub}}+1)/2, \quad k = A/B,$$

and

$$k' = \sqrt{1-k^2}.$$

Equation (18) models a line with center conductor width A and separation between ground lines B, as shown in Fig. 13. The lines are modeled on a silicon half-plane with relative permittivity ϵ_{sub}. The effective relative permittivity ϵ_{eff} of the transmission line is treated as the average of the free-space and substrate relative permittivities, and the function K represents the complete elliptic integral of the first kind. The transmission line can be treated as being immersed in a single dielectric of relative permittivity ϵ_{eff} with characteristic impedance $Z_0 = \sqrt{\epsilon_{\mathrm{eff}}}/(cC_t)$, where c is the speed of light in free space.[26] Because the characteristic impedance of a low-loss transmission line also is $Z_0 = \sqrt{L_t/C_t}$, the inductance per unit length L_t can be calculated using the previous expressions for C_t and Z_0. Using the parameters in Table III and Eq. (18), the predicted capacitance and inductance per unit length are 118 pF/m and 596 nH/m, respectively. The predicted characteristic impedance Z_0 of the unloaded line is 71 Ω.

TABLE III. Additional parameters and dimensions for the calculation of unloaded coplanar waveguide impedance Z_0.

Parameter	Symbol	Value
Center conductor width	A	20 μm
Ground conductor separation	B	100 μm
Silicon substrate relative permittivity	ϵ_{sub}	11.7
Speed of light	c	3.0×10^8 m/s

The propagation constant in rad/m of an unloaded rf transmission line is $2\pi f_c\sqrt{L_tC_t}$. To determine the effects of the capacitive loading by the membranes, the total length of the unloaded transmission line can be viewed as a composite of N sections of line, each of length d. The phase length of the capacitively loaded transmission line is calculated by incorporating a single membrane capacitor into each section of the lumped, reactive transmission line model shown in Fig. 14. Thus, the total radian phase length of the loaded line becomes

$$\Phi = 2\pi f_c N\sqrt{L_t d(C_t d + C_m)}. \tag{19}$$

To calculate the phase shift $\Delta\Phi$ due to changes in membrane capacitance, the phase length of the line, loaded with capacitance C_m, is subtracted from that loaded with $C_m+\Delta C_m$, as shown below:

$$\Delta\Phi = 2\pi f_c N[\sqrt{L_t d(C_t d + C_m + \Delta C_m)} - \sqrt{L_t d(C_t d + C_m)}]. \tag{20}$$

However, a simpler approximate expression for $\Delta\Phi$ can be obtained in terms of the characteristic impedance of the loaded transmission line impedance Z_L. Differentiating Eq. (19) with respect to C_m and linearizing the expression for small changes in capacitance yields

$$\Delta\Phi \approx \frac{\pi f_c N\sqrt{L_t d}}{\sqrt{C_t d + C_m}}\Delta C_m . \tag{21}$$

Because the characteristic impedance of the low-loss, capacitively loaded transmission line is given by

$$Z_L = \sqrt{\frac{L_t d}{C_t d + C_m}}, \tag{22}$$

Eq. (21) simplifies to

$$\Delta\Phi \approx \pi f_c N Z_L \Delta C_m . \tag{23}$$

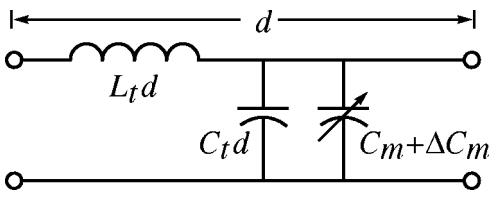

FIG. 14. The lumped-element, lossless model of a single section of loaded transmission line, including the capacitive membrane.

TABLE IV. Simulated and measured parameters for the phase shift calculations.

Parameter	Symbol	Value
Capacitance of unloaded line[a]	C_t	118 pF/m
Inductance of unloaded line[a]	L_t	596 nH/m
Membrane static capacitance[a]	C_m	79 fF
Change in membrane capacitance[a]	ΔC_m	4.3 aF
Number of sections	N	45
Length of each section	d	206 μm
Carrier frequency	f_c	2.8 GHz

[a]Calculated from previous formulas.

This expression can be used to compute the phase shift due to a fluctuation in membrane capacitance ΔC_m and predicts that the phase shift is proportional to ΔC_m, the loaded transmission line impedance Z_L, the number of membranes N, and the rf carrier frequency f_c.

Using either Eqs. (20) or (23) and the fabricated microphone parameters and previously calculated values given in Table IV, the expected phase shift amplitude is 58.6 μrad for 1 Pa rms acoustic pressure. The calculated loaded line impedance from Eq. (22) is 34.5 Ω. This impedance is sufficiently similar to the typical 50-Ω impedances of other rf circuit components to obviate the need for impedance-matching networks in the phase detection circuit.

D. Phase detection

The mixer in the phase detection circuit converts the phase shift to a voltage, assuming the input signals are in quadrature. The detection constant K_d of the mixer, first introduced in Eq. (3), is a function of the mixer loss, the rf frequency, the terminating impedance, and the rf power level at the mixer inputs.[19] Although K_d can be measured directly in the phase detection circuit, an estimate of K_d is useful for the simulation model.

The voltage amplitude of a rf signal on a transmission line with impedance Z_L is $\sqrt{2Z_L P_c}$, where P_c is the rf carrier power at the output of the microphone or at the input to the mixer. Assuming perfect impedance matching and taking L_m as the mixer conversion loss, defined as the ratio of power available from the rf port to the power delivered to the output, the voltage at the rf port is reduced by a factor of $\sqrt{L_m}$ at the mixer output. Therefore, the detection constant K_d in V/rad is approximately

$$K_d \approx \sqrt{\frac{2Z_L P_c}{L_m}}. \tag{24}$$

This expression assumes that sufficient drive power is available at the mixer LO port to fully switch the mixer diodes. Furthermore, it does not account for any impedance mismatch at the mixer ports nor does it account for saturation or compression of the output signal for large rf powers. Therefore, for a low-loss microphone transmission line, as is the case here, the input rf power that saturates the mixer should be substituted for P_c. This sets the upper limit for K_d. Using experimentally determined values for the mixer of 7 dB for conversion loss and 7 dB m for the input power compression, as shown in Table V, the estimated mixer detection constant is 0.263 V/rad.

TABLE V. Simulated and measured parameters for the mixer phase detection constant K_d.

Parameter	Symbol	Value
Loaded line impedance[a]	Z_L	34.5 Ω
rf power (saturation)[b]	P_c	5.0 mW (7 dBm)
Conversion loss[b]	L_m	5.0 (7 dB)

[a]Calculated from the previous formulas.
[b]Experimentally measured in the phase detection circuit.

E. Baseband amplification

The output voltage amplitude from the mixer is 15.4 μV, using a calculated phase shift amplitude of 58.6 μrad for 1 Pa rms. Because this demodulated voltage signal is small, a baseband amplifier is necessary to increase the magnitude of the voltage signal before further signal processing or digitization. An amplifier providing 60.0 dB of gain brings the signal level to 15.4 mV, or 10.9 mV rms. Fortunately, the low output impedance of the rf mixer in the phase detection circuit allows for such an amplification with only a slight degradation to the SNR. The noise considerations of the amplifier and of the entire system are considered in the following sections.

F. Mechanical noise

Acoustic transducers are subject to thermal mechanical noise from the acoustic medium. This mechanical noise is often referred to as acoustic self-noise,[23] since it is a property of the microphone's structural design and is unrelated to the electrical detection system. In many microphones, the squeeze-film damping due to air flow through the acoustic holes in the backplate and through the pressure equalization vent is the dominant noise mechanism for the entire system over most of the audio frequency range.[27,28] Furthermore, experiments by Zuckerwar and Ngo[29] suggest that the mechanical $1/f$ noise of an unsealed microphone structure also correlates with the air gap resistance. As there is no acoustic flow behind a vacuum-sealed CMUT membrane, the structure has a much lower mechanical noise floor than that of an unsealed structure. This is evident in the equivalent circuit model of the CMUT by the absence of many acoustical resistances, which represent dissipation mechanisms in the structure. As seen in Fig. 4, the remaining dissipation mechanism in a sealed membrane structure is represented by the radiation resistance. This thermal noise due to acoustic radiation of the moving membranes is experienced by all microphones that are exposed to the air.

A common approach to calculating the pressure noise of small sensors, originally undertaken by Sivian and White,[30] is to calculate the pressure noise from the radiation of a piston in an infinite baffle. Fellgett,[31] however, notes that the infinite-baffle assumption leads to a factor-of-2 discrepancy and is not the usual configuration for a miniature microphone. A more general approach examines the intrinsic ther-

mal noise of the medium, derived by Hunt.[32] The resulting mean-square pressure fluctuation noise in a 1-Hz band is

$$\overline{p^2} = \frac{4\pi k_B T_0 \rho_a f_a^2}{c_a}, \tag{25}$$

where k_B is Boltzmann's constant (1.38×10^{-23} J/K), T_0 is the absolute temperature of the system, ρ_a is the density of air, c_a is the speed of sound in air, and f_a is the acoustic frequency. Taking the square root of Eq. (25) yields the rms pressure fluctuations per $\sqrt{\text{Hz}}$, valid for a sensor that is smaller than the wavelength of sound at the frequencies of interest. Integrating the A-weighted rms pressure noise yields an equivalent self-noise of -9.3 dB(A) SPL at standard pressure and room temperature. As the mechanical noise due to radiation is small, it does not impose practical limits on the sensitivity of a miniature microphone composed of otherwise lossless, vacuum-sealed CMUT membranes. Therefore, mechanical noise can be neglected in simulations since the electrical noise dominates.

G. Electrical noise

There are several sources of electrical noise in the phase detection electronics that must be considered. First, the oscillator, which serves as the rf signal source in Fig. 6, contributes phase noise to the circuit. This phase noise is present in both the microphone and the reference branches of the detection circuit. For similar time delays in the two circuit branches, it is largely correlated at the rf and LO inputs of the mixer. Therefore, most of the oscillator phase noise cancels at the mixer output for a low-noise signal source, such as a dielectric resonator oscillator, and the phase noise of the signal source can be neglected in this model. For acoustic frequencies below 100 kHz, we have experimentally confirmed that the noise floor of the detection circuit does not change with high-quality oscillators of varying spectral purities.

The dominant source of noise in rf detection is due to thermal noise, shot noise in the mixer diodes, and $1/f$ noise.[19] The white noise floor of the mixer is modeled using the mixer's single sideband noise figure F_m and the mixer's conversion loss L_m. The available noise power in W/Hz at the mixer output is given by

$$N_m = \frac{k_B T_0 F_m}{L_m}, \tag{26}$$

which has a flat acoustic spectrum. Assuming a matched termination of R_0 at the mixer output, the expected rms output voltage per $\sqrt{\text{Hz}}$ is

$$v_{m,N} = \sqrt{\frac{k_B T_0 F_m R_0}{L_m}}. \tag{27}$$

In addition to white noise with a flat spectral density, realistic mixers also have a component that varies approximately as $1/f$. Equation (27) can be modified to account for this noise by defining a corner frequency $f_{1/f}$ as the baseband or acoustic frequency f_a at which the $1/f$ component of the noise equals the mixer's white noise floor:

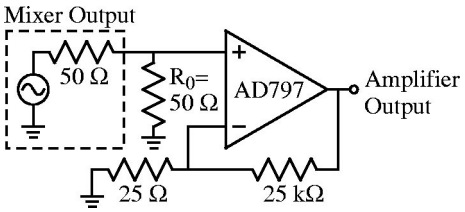

FIG. 15. Schematic of the baseband amplifier, along with the 50-Ω source resistance of the mixer, seen through the low-pass filter of the previous stage.

$$v_{m,N} = \sqrt{\frac{k_B T_0 F_m R_0 (1 + f_{1/f}/f_a)}{L_m}}. \tag{28}$$

The $1/f$ noise corner frequency depends on the rf frequency, the power levels in the circuit, and the cleanliness of the semiconductor fabrication facility for the Schottky diodes in the mixer.[33,34] This makes estimation of the $1/f$ corner frequency difficult without specific information about the mixer diodes and how the mixer's $1/f$ noise is influenced by external circuit components. Thus, the noise performance of a specific mixer in the phase detection circuit is best determined experimentally. Although lower noise performance is possible, a typical value for the corner frequency $f_{1/f}$ in rf double-balanced mixers is 100 kHz.[35] In the absence of further information, a value of 100 kHz is assumed for $f_{1/f}$ in sample noise calculations to illustrate the effects of mixer $1/f$ noise on system performance.

The baseband amplifier contributes thermal electrical noise and, below 100 Hz, excess $1/f$ noise, which is neglected in the model. Because the output impedance of the mixer and low-pass filter combination is low, near 50 Ω, the effects of the current noise contributed by the baseband amplifier are usually negligible. Therefore, an amplifier with high current noise may be used as long as the voltage noise is very low. Figure 15 shows the schematic of the baseband amplifier with feedback resistors, set for a voltage gain of 1001 or 60.0 dB. The 50 Ω resistor at the positive terminal serves as the terminating load for the mixer, R_0, which itself has an output impedance near 50 Ω. Although the matched termination reduces the signal level at the input of the amplifier, experimental measurements show that it also reduces the noise floor and the dc offsets from the mixer for an overall improvement in the SNR.

For the resistor values of Fig. 15 and the parameters in Table VI, the baseband amplifier noise figure is 3 dB, or a factor of 2.0, calculated using a source resistance of 50 Ω from the previous stage. Figure 16 shows the calculated electrical noise at the output of the baseband amplifier that is due to the mixer and the amplifier. The simulation suggests that the mixer's $1/f$ noise dominates the total output noise of the detection circuit over the audio range.

H. Calculating sensitivity

An estimate of the sensitivity can be obtained with the models developed for calculating the signal and noise levels of the microphone and its phase detection circuit. The predicted signal after amplification is -39.2 dB relative to 1 V rms for a 1 Pa rms acoustic signal and is independent of the

TABLE VI. Additional parameters for simulating the electrical noise from the mixer and amplifier at the amplifier output.

Parameter	Symbol	Value
Terminating resistance	R_0	50 Ω
Mixer noise figure[a]	F_m	5.0 (7 dB)
Mixer 1/f corner frequency[b]	$f_{1/f}$	100 kHz
Op-amp input voltage noise[c]		0.9 nV/Hz
Op-amp input current noise[c]		2.0 pA/Hz
Boltzmann's constant	k_B	1.38×10^{-23} J/K
System temperature	T_0	293 K

[a]Typical manufacturer's specifications for Marki Microwave M1-0204 NA mixer.
[b]A typical value for rf mixers (Ref. 35).
[c]Typical manufacturer's specifications for the Analog Devices AD797 operational amplifier.

acoustic frequency below 100 kHz. The predicted noise level at 1 kHz is -106.7 dB V rms per $\sqrt{\text{Hz}}$ from the simulation shown in Fig. 16. Therefore, the predicted SNR in a 1 Hz noise bandwidth at 1 kHz is 67.5 dB for 1 Pa rms of pressure. Referring the integrated, A-weighted output noise to the pressure input of the microphone yields a predicted equivalent noise level of 61.9 dB(A) SPL over the audio band.

The model's prediction of the signal level is most sensitive to the membrane thickness l_m, as this determines the membrane's static deflection and the effective capacitor gap spacing. Due to nonuniformities across the wafer, the estimated uncertainty in the measurement membrane film thickness is ±5 nm. Recalculating the signal level using the maximum range of 0.395 to 0.405 μm for l_m, the predicted output signal ranges from -38.0 to -40.4 dB V rms for an uncertainty of up to 2.4 dB in the model's prediction for a signal level.

V. EXPERIMENTAL RESULTS

Acoustic characterization of the CMUT microphone with rf detection is performed in an anechoic chamber, using a Brüel & Kjær Type 4135 1/4 in. free-field microphone as the reference microphone. The reference microphone is positioned 1 cm above the microphone under test, both oriented toward the speaker for normal incidence. The reference microphone is calibrated at 1 kHz using an ACO Pacific 511E Sound Level Calibrator for 94 dB SPL, or 1 Pa rms. Following the calibration of the reference microphone, both microphones are exposed to the same 1 kHz sound field. A comparison of the relative output signals between the reference and test microphones determines the response of the CMUT microphone with rf detection, which is -42.7 dB V rms for 1 Pa rms of pressure.

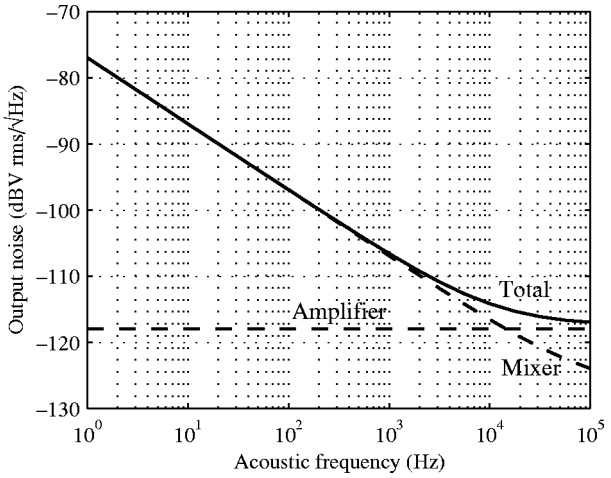

FIG. 16. Simulated total voltage noise (solid line) at amplifier output as a function of acoustic frequency, separated into components (dashed lines) due to the mixer and amplifier.

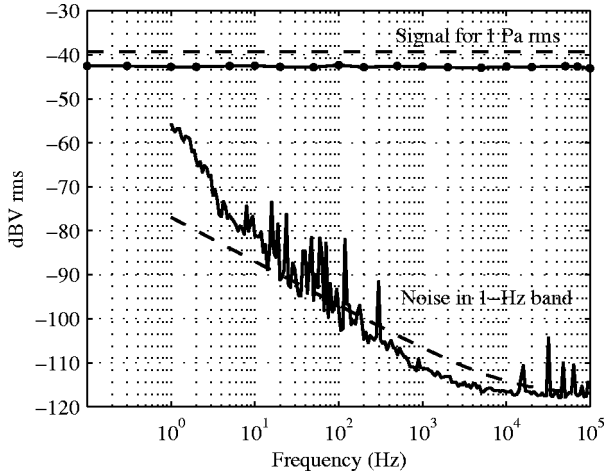

FIG. 17. Measured (solid) and simulated (dashed) output signal for 1 Pa rms and output noise voltage in a 1 Hz band. The signal response is measured using voltage actuation and correlated to the acoustic measurement at 1 kHz.

Acoustic testing over many decades of frequency is difficult without specialized low- and high-frequency microphones and sound sources. An alternative method of testing the frequency response uses electrostatic actuation of the CMUT membranes at infrasonic through ultrasonic frequencies. This method captures the response of the microphone and rf detection system to the force or pressure at the surface of the membranes, but does not account for acoustic diffraction effects of the microphone. The application of voltage actuation signal and dc bias is accomplished by inserting a bias T before and after the microphone in the circuit in Fig. 6. To compensate for the variations in response of the bias T with frequency, the actuation voltage applied to the input of the bias T is adjusted at each frequency to maintain a constant ac voltage on the capacitive membranes of the microphone.

The frequency of voltage actuation is varied from 0.1 Hz to 100 kHz, while maintaining a 5.8-V dc bias and a 68-mV amplitude excitation on the membrane capacitors. This voltage bias and excitation are both small enough to prevent an electrostatic collapse of the membrane while producing an output signal, -11.0 dB V rms, that is much larger than the noise floor. The output signal of the microphone and detection circuitry varies less than 0.5 dB over six decades of frequency, from 0.1 Hz to 100 kHz. The previous acoustic measurement at 1 kHz correlates the output under voltage actuation with that from pressure excitation, generating the frequency response plot in Fig. 17. The predicted response curves use the simulation models developed in Sec. IV with the parameters for the fabricated microphone and phase detection circuit.

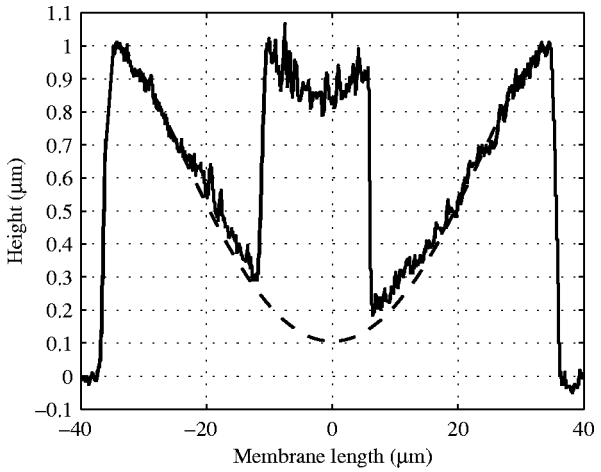

FIG. 18. Measured (solid line) AFM profile of a membrane from the fabricated microphone, compared to the calculated profile (dashed line) from Eq. (11). The patterned metal transmission line causes the step in the measured profile. The 70-μm scan path along the membrane length corresponds to the x coordinate axis of Fig. 10.

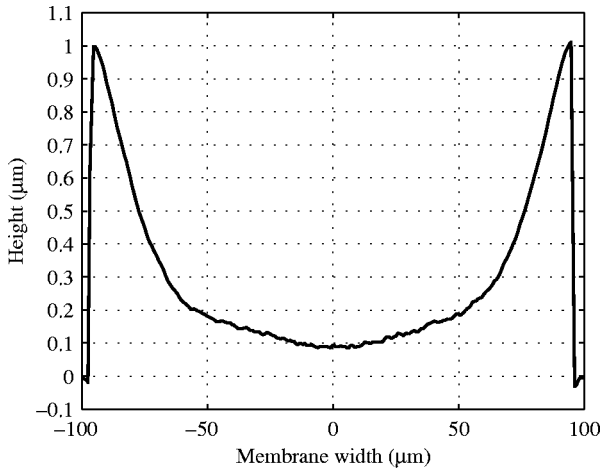

FIG. 19. Measured optical interferometer profile of a membrane from the fabricated device along the metal transmission line. The 190-μm profile of membrane width corresponds to the y-coordinate axis of Fig. 10.

The output voltage noise of the microphone in the phase detection circuit is measured with a fast Fourier transform (FFT) spectrum analyzer (Stanford Research Systems model SR760). Figure 17 shows the measured output noise floor of the microphone with its detection circuitry measured in a laboratory environment. At 1 kHz, the measured noise is $-111.1\,\mathrm{dB}/\sqrt{\mathrm{Hz}}$ relative to 1 V rms. Therefore, the measured SNR at 1 kHz is 68.4 dB/Pa rms in a 1-Hz noise band. The measured signal and noise plots of Fig. 17 correspond to an A-weighted equivalent noise level of 63.6 dB(A) SPL for the microphone.

VI. DISCUSSION

A. Model verification and comparison

The measured acoustic response of the microphone at 1 kHz is 3.5 dB lower than that predicted by the model, and the measured noise level at 1 kHz is 4.4 dB lower than predicted. Both of the measurements are slightly out of the range of expected error based on uncertainties in thickness and $1/f$ corner frequency. However, some additional measurements of membrane deflection, the rf transmission line, and the mixer lend insight as to the probable sources of error in the simulation model.

Accurate modeling of the membrane deflection under atmospheric pressure is important because the capacitance calculations are sensitive to the electrode spacing. Fortunately, u_{dc} can be verified on the fabricated microphone. An atomic force microscope (AFM; Digital Instruments Dimension 3000), scanning along the membrane's length, generates the profile shown in Fig. 18. Subtracting the 0.71-μm metal line thickness yields a peak membrane deflection of approximately 0.89 μm, which is similar to the predicted peak deflection of 0.895 μm. The profile along the membrane width, shown in Fig. 19, is measured optically since the metal signal line is reflective over the entire scan. An optical interferometer (Zygo White-Light 3D Surface Profiler) measures a peak static deflection of 0.91 μm, slightly greater than predicted. Both measurements verify the initial gap height of 1.00 μm. Since both the AFM and optical interferometer measurements of u_{dc} are very similar to the predicted deflection, no adjustments to this part of the model are necessary. Although the static deflection of the membrane is easily verified, the ac displacement amplitude u_{ac} is too small for us to accurately determine, even when using voltage excitation of the membranes to increase the measurable movement. Therefore, an error in the prediction of u_{ac} by Eq. (13) could account for the larger predicted signal level than measured.

Although the output signal is not particularly sensitive to the impedance or loss of the microphone transmission line structure, rf measurements provide another verification of the transmission line aspects of the model. Measurements at 2.8 GHz using a network analyzer (Hewlett-Packard model 8510C with 8517A S-parameter test set) indicate the characteristic impedance of the transmission line structures. An unloaded coplanar waveguide with the same dimensions as those of the fabricated microphone has a characteristic impedance Z_0 of 78 Ω, similar to the predicted value of 71 Ω for the dimensions shown in Table III. The higher measured impedance of the line is likely due to the finite extent of the ground conductors of the unloaded coplanar waveguide, as expected from more elaborate transmission line models.[36] The measured impedance of the loaded transmission line of the fabricated microphone is 37 Ω, only slightly larger than the predicted loaded impedance of 34.5 Ω. The measured transmission line loss on the microphone device is 4.1 dB at 2.8 GHz. The loss is higher than that of other published coplanar lines on silicon,[22] but this is likely due to the capacitive loading as well as the thin, 0.71 μm aluminum metalization and step coverage over the membranes. Nonetheless, this loss still is small enough to be neglected in the calculation of the mixer detection constant K_d, as there still is sufficient rf power at mixer to saturate it.

The model for mixer detection constant K_d is verified experimentally for the specific mixer in our phase detection circuit at 2.8 GHz. A 50-Ω step attenuator replaces the microphone in the phase detection circuit of Fig. 6 to vary the amount of rf power P_c at the mixer. The detection constant is measured by recording and scaling the output voltage for

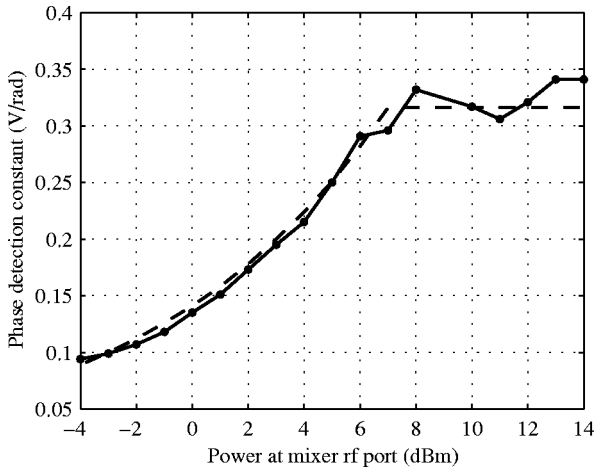

FIG. 20. Mixer phase detection constant K_d measurement (solid line) and model (dashed line). The model assumes 7 dBm of conversion loss, 7 dBm of saturation power, and 50 Ω for the line impedance.

small departures in phase from quadrature, using a micrometer-drive phase shifter. As shown in Fig. 20, the measured K_d conforms to that predicted by Eq. (24) if one assumes 7 dB for the conversion loss L_m, 7 dBm saturation power for P_c, and 50 Ω for the line impedance Z_L. Replacing the step attenuator with the fabricated microphone permits direct measurement of 0.27 V/rad for K_d for this microphone. As the measurement is similar to the simulation value of 0.263, the calculation of K_d is not a cause of the observed discrepancy between the measurement and the model.

One likely cause for the overestimate of the signal level in the simulation model is evident from the deflection profile along membrane width in Fig. 19. The one-dimensional membrane and capacitance models assume that the dc and ac deflections along the membrane width W remain constant over the ground electrode width w_g. For the device tested, w_g extends between ± 50 μm along the width in the profile of Fig. 19. Since the membrane deflection decreases over this region of W, the one-dimensional simplification to model diaphragm motion overestimates the capacitances C_m and ΔC_m in the model. The larger calculated value for C_m also explains why the predicted impedance of the loaded transmission line is lower than measured, since a larger loading capacitance decreases the line impedance. A second possible source of error in the prediction for signal level arises from nonlinear stress-stiffening effects in the membranes, which are neglected in the equations for dc and ac membrane response. As the membrane deflects under atmospheric pressure, the tensile stress of the structure increases, thereby increasing the stiffness of the structure and reducing the incremental ac motion of the membrane. A more accurate model might use finite element simulations to calculate the two-dimensional membrane deflection profile and capacitance, including stress-stiffening effects. This method potentially reduces both of the likely sources of error in the simulation model, although the model complexity and necessary computation time increase with finite element simulations. For analyzing tradeoffs or for developing optimal microphone designs, the closed-form, one-dimensional solution to the membrane response may be preferable if some error can be tolerated.

TABLE VII. A summary of measured parameters for the fabricated microphone and its detection circuitry, compared to those predicted by the model for a 1 Pa rms signal.

Parameter	Predicted	Measured
Static deflection (μm)	0.895	0.89–0.91
Unloaded line impedance (Ω)	71	78
Loaded line impedance (Ω)	34.5	37
Detection constant (V/rad)	0.263	0.27
Output signal (dB V rms)	−39.2	−42.7
Equivalent noise level [dB(A) SPL]	61.9	63.6

The measured noise floor of Fig. 17 indicates the presence of ambient acoustic noise in the audio band. In addition, there are several peaks in the noise floor at multiples of 16 kHz. The high-frequency peaks could be due to electromagnetic interference with the rf detection circuitry, with regular multiples created by mixing products. The simple $1/f$ noise model of the mixer overestimates the noise at higher frequencies and underestimates the noise at very low frequencies. Below 10 Hz, the measured noise varies almost as $1/f^2$. Other measurements of $1/f$ noise in diodes suggest that the noise exhibits a dependence of $1/f^{\alpha}$, where α is slightly greater than unity.[37] As previously discussed, $1/f$ noise is difficult to predict because its dependence on several factors, internal and external to the mixer, is unknown. Table VII summarizes and compares selected measurements with the model predictions.

B. Improving sensitivity

The use of sealed CMUT membranes in the microphone provides a uniform, wideband response to pressure while sealing out particle contamination and moisture. Improving the SNR of the microphone is a remaining design challenge, as the use of relatively small, stiff membranes reduces the sensor's mechanical response to pressure. Some possible approaches for reducing the stiffness of the membranes include corrugated structures or a reduction of the membrane material's residual stress through doping and annealing.[38] The use of larger, unsealed membranes that are not fully supported along their perimeters also may increase the membrane motion though some of the advantages in bandwidth, frequency response, and durability may be forfeited.

Some unique opportunities for improvement exist with the described rf detection technique, without necessarily modifying the sealed membrane structure. Since the loaded transmission line translates the capacitance variations of the membranes into phase variations, methods that increase the phase modulation of the rf carrier or reduce the noise of the phase detection electronics also have the potential to improve the sensing capability of the microphone. For example, the use of higher rf frequencies increases the phase shift of the rf carrier that travels along the microphone transmission line. Because the phase shift is proportional to f_c, as shown in Eq. (23), each doubling of frequency increases the signal level by up to 6 dB if K_d remains unchanged. However, the optimum rf frequency balances the increase in phase shift

with the increases in rf loss through the transmission line structure and any increase in the noise floor of the detection electronics at higher operating frequencies.

In addition to increasing the phase shift of the rf carrier, the resolution of the phase detection circuitry also can be improved. More sophisticated circuit topologies suppress the carrier through an rf interferometer, as demonstrated by Sann.[39] Because the suppressed carrier prevents saturation of the mixer, it is possible to amplify the phase modulation signal at rf frequencies prior to the mixer, which introduces most of the electrical noise. Since low-noise, narrowband amplifiers are available at rf frequencies, the effects of the mixer $1/f$ noise and baseband amplifier noise are mitigated, and the system noise floor can approach that of fundamental electrical thermal noise limits. Ivanov *et al.*[40] demonstrate such a phase detection system capable of measuring rms phase variations at 1 kHz of $0.3\,\mathrm{nrad}/\sqrt{\mathrm{Hz}}$, using a carrier frequency of 9 GHz and the same rf power level as our circuit. For comparison, the phase detection circuit presented here is capable of measuring rms phase variations of $17\,\mathrm{nrad}/\sqrt{\mathrm{Hz}}$ at 1 kHz, based on the measured SNR of Fig. 17 using a calculated rms phase variation of 41.4 μrad. This suggests that up to 35 dB improvement in SNR at 1 kHz may be possible through carrier-suppressed phase detection topologies. The potential improvement is greater at lower audio and infrasonic frequencies.

VII. CONCLUSIONS

The use of the sealed CMUT membrane as the mechanical structure for a microphone provides a uniform, wideband response while sealing out moisture. In rf detection, the small capacitance variations of the membranes along a transmission line are sensed through the phase variations of a rf carrier. The mathematical model presented here predicts a SNR of 67.5 dB/Pa rms at 1 kHz in a 1-Hz band, compared to a measured SNR of 68.4 dB for the fabricated microphone. Over the audio bandwidth, the measured sensitivity corresponds to an equivalent noise level of 63.6 dB(A) SPL. Electrostatic actuation of the membrane demonstrates the potential bandwidth of the microphone, which exhibits less than 0.5 dB of variation in the output response of the system from 0.1 Hz to 100 kHz.

While various rf or carrier-based methods have been applied to other microphones, to the authors' knowledge such techniques previously have not been applied to sealed membrane structures such as the CMUT. As the mechanical noise of the condenser structure ultimately limits the minimum detectable pressure that can be sensed, applying a sensitive electrical detection technique to a conventional micromachined microphone may offer little or no improvement to the microphone's sensing capability. However, the combination of a sensitive rf technique and a sealed membrane structure extends the range of possible sensitivities for micromachined microphones. The rf detection technique presented here translates variations in membrane capacitance into phase variations of a rf signal, which can be measured extremely accurately. Therefore, the use of sealed CMUTs in conjunction with rf detection offers the potential to surpass the sensitivity of other micromachined microphones, which often are limited by their structural mechanical noise, while retaining advantages such as a uniform, wideband response and protection from moisture.

ACKNOWLEDGMENTS

This work is supported by the Defense Advanced Research Projects Agency's Microsystems Technology Office. The microphone was fabricated at the Stanford Nanofabrication Facility, which is supported in part by the National Science Foundation. The authors also wish to thank Nino Srour, Michael Scanlon, and their colleagues at the Army Research Laboratory for their assistance in testing the microphone.

[1] P. Scheeper, A. van der Donk, W. Olthuis, and P. Bergveld, "A review of silicon microphones," Sens. Actuators, A **44**, 1–11 (1994).
[2] S. Bouwstra, T. Storgaard-Larsen, P. Scheeper, J. O. Gulløv, J. Bay, M. Müllenborg, and P. Rombach, "Silicon microphones—a Danish perspective," J. Micromech. Microeng. **8**, 64–68 (1998).
[3] N. Masuzawa and E. Ohdaira, "Information contained in the radiating ultrasound during ultrasonic welding," Ultrasonics **38**, 609–613 (2000).
[4] N. Versfeld and J. Vos, "Annoyance caused by sounds of wheeled and tracked vehicles," J. Acoust. Soc. Am. **101**, 2677–2685 (1997).
[5] C. Birkett, E. Shalis, N. Vlahopoulos, and Z. Wu, "Numerical load generation, vibration analysis, and acoustic signature prediction of a ground vehicle," in *Proceedings of the National Conference on Noise Control Engineering* (Inst. of Noise Control Engineering, University Park, PA, 1997), Vol. 1, pp. 123–128.
[6] A. Bedard, Jr. and T. Georges, "Atmospheric infrasound," Phys. Today **53**, 32–37 (2000).
[7] R. K. Cook and A. Bedard, Jr., "On the measurement of infrasound," Geophys. J. R. Astron. Soc. **26**, 5–11 (1971).
[8] A. J. Zuckerwar, "Principles of operation of condenser microphones," in *AIP Handbook of Condenser Microphones: Theory, Calibration, and Measurements*, edited by G. S. K. Wong and T. F. W. Embleton (AIP Press, New York, 1995), Chap. 3, pp. 37–69.
[9] M. Hibbing, "High-quality RF condenser microphones," in *Microphone Engineering Handbook*, edited by M. L. Gayford (Focal Press, Oxford, 1994), Chap. 4, pp. 158–186.
[10] A. S. Ergun, A. Atalar, B. Temelkuran, and E. Özbay, "A new detection method for capacitive micromachined ultrasonic transducers," Appl. Phys. Lett. **72**, 2957–2959 (1998).
[11] A. S. Ergun, B. Temelkuran, E. Özbay, and A. Atalar, "A new detection method for capacitive micromachined ultrasonic transducers," IEEE Trans. Ultrason. Ferroelectr. Freq. Control **48**, 932–942 (2001).
[12] A. van der Donk, P. Scheeper, W. Olthuis, and P. Bergveld, "Modelling of silicon condenser microphones," Sens. Actuators, A **40**, 203–216 (1994).
[13] L. L. Beranek, *Acoustics* (Acoustical Society of America, Woodbury, NY, 1996), Chap. 6, pp. 144–182.
[14] P. R. Scheeper, "A silicon condenser microphone: Materials and technology," Ph.D. thesis, University of Twente, 1993, pp. 23–25.
[15] M. I. Haller and B. T. Khuri-Yakub, "A surface micromachined electrostatic ultrasonic air transducer," IEEE Trans. Ultrason. Ferroelectr. Freq. Control **43**, 1–6 (1996).
[16] I. Ladabaum, X. C. Jin, H. T. Soh, A. Atalar, and B. T. Khuri-Yakub, "Surface micromachined capacitive ultrasonic transducers," IEEE Trans. Ultrason. Ferroelectr. Freq. Control **45**, 678–690 (1998).
[17] V. Tarnow, "Thermal noise in microphones and preamplifiers," Brüel & Kjær Tech. Rev. **3**, 3–14 (1972).
[18] D. M. Pozar, *Microwave Engineering*, 2nd ed. (Wiley, New York, 1998), Chap. 8, pp. 422–493.
[19] F. Walls, A. Clements, C. Felton, M. Lombardi, and M. Vanek, "Extending the range and accuracy of phase noise measurements," in *Proceedings of the 42nd Annual Symposium on Frequency Control* (IEEE, Baltimore, MD, 1988), pp. 432–441.
[20] N. S. Barker and G. M. Rebeiz, "Distributed MEMS true-time delay phase shifters and wide-band switches," IEEE Trans. Microwave Theory Tech. **46**, 1881–1890 (1998).

[21] X. Jin, ''Micromachined capacitive ultrasonic immersion transducer array,'' Ph.D. thesis, Stanford University, 2002, Chap. 4, pp. 51–71.
[22] A. C. Reyes, S. M. El-Ghazaly, S. J. Dorn, M. Dydyk, D. K. Schroder, and H. Patterson, ''Coplanar waveguides and microwave inductors on silicon substrates,'' IEEE Trans. Microwave Theory Tech. **43**, 2016–2022 (1995).
[23] L. L. Beranek, *Acoustical Measurements*, revised ed. (American Institute of Physics, Cambridge, MA, 1993), Chap. 5, pp. 177–265.
[24] W. P. Mason, in *Electromechanical Transducers and Wave Filters* (Van Nostrand, New York, 1948), Chap. 5, pp. 158–184.
[25] M. H. Badi, G. G. Yaralioglu, A. S. Ergun, S. T. Hansen, E. J. Wong, and B. T. Khuri-Yakub, ''Capacitive micromachined ultrasonic lamb wave transducers using rectangular membranes,'' IEEE Trans. Ultrason. Ferroelectr. Freq. Control **50**, 1191–1203 (2003).
[26] C. P. Wen, ''Coplanar waveguide: A surface strip transmission line suitable for nonreciprocal gyromagnetic device application,'' IEEE Trans. Microwave Theory Tech. **17**, 1087–1090 (1969).
[27] S. C. Thompson, J. L. LoPresti, E. M. Ring, H. G. Nepomuceno, J. J. Beard, W. J. Ballad, and E. V. Carlson, ''Noise in miniature microphones,'' J. Acoust. Soc. Am. **111**, 861–866 (2002).
[28] T. B. Gabrielson, ''Mechanical-thermal noise in micromachined acoustic and vibration sensors,'' IEEE Trans. Electron Devices **40**, 903–909 (1993).
[29] A. J. Zuckerwar and K. C. T. Ngo, ''Measured $1/f$ noise in the membrane motion of condenser microphones,'' J. Acoust. Soc. Am. **95**, 1419–1425 (1994).
[30] L. J. Sivian and S. D. White, ''On minimum audible sound fields,'' J. Acoust. Soc. Am. **4**, 288–321 (1933).
[31] P. B. Fellgett, ''Thermal noise limits of microphones,'' J. Inst. Electron. Radio Eng. (UK) **57**, 161–166 (1987).
[32] F. V. Hunt, ''Propagation of sounds in fluids,'' in *American Institute of Physics Handbook*, edited by D. E. Gray, 3rd ed. (McGraw-Hill, New York, 1972), Sec. 3c-11, pp. 65–68.
[33] A. Yoginder and W. J. Moroney, ''Microwave mixer and detector diodes,'' Proc. IEEE **59**, 1182–1190 (1971).
[34] S. Marki (*private communication*, Marki Microwave, Morgan Hill, CA, 2002).
[35] S. Spohrer (*private communication*, Miteq, Hauppauge, NY, 2001).
[36] G. Ghione and C. U. Naldi, ''Coplanar waveguides for MMIC applications: Effect of upper shielding, conductor backing, finite-extent ground planes, and line-to-line coupling,'' IEEE Trans. Microwave Theory Tech. **35**, 260–267 (1987).
[37] R. J. King, *Microwave Homodyne Systems* (Peter Peregrinus, Stevenage, England, 1978), Chap. 4, pp. 78–105.
[38] J. Miao, R. Lin, L. Chen, Q. Zou, S. Y. Lim, and S. H. Seah, ''Design considerations in micromachined silicon microphones,'' Microelectron. J. **33**, 21–28 (2002).
[39] K. H. Sann, ''The measurement of near-carrier noise in microwave amplifiers,'' IEEE Trans. Microwave Theory Tech. **16**, 761–766 (1968).
[40] E. N. Ivanov, M. E. Tobar, and R. A. Woode, ''Microwave interferometry: Application to precision measurements and noise reduction techniques,'' IEEE Trans. Ultrason. Ferroelectr. Freq. Control **45**, 1526–1536 (1998).
[41] G. S. Kino, *Acoustic Waves: Devices, Imaging, and Analog Signal Processing* (Prentice–Hall, Englewood Cliffs, NJ, 1987), pp. 548–562.